NLR-TP-2002-289

Material-based failure analysis of a helicopter rotor hub
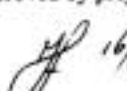## Revised edition

R.J.H. Wanhill

This report has been prepared in the format required for the Journal Practical Failure Analysis.

Approved by author:	Approved by project manager:	Approved by project managing department:
W 25/03/2003	16/4	H₂O 28/4

Summary

A Lynx helicopter from the Royal Netherlands Navy lost a rotor blade during preparation for take-off. The blade loss was due to failure of a rotor hub arm by fatigue. The arm was integral to the titanium alloy rotor hub. An extensive material-based failure analysis covered the hub manufacture, service damage and estimates of service stresses. There was no evidence for failure owing to poor material properties. However, fractographic and fracture mechanics analyses of the service failure, a full-scale test failure and specimen test failures indicated that the service fatigue stress history could have been more severe than anticipated. This possibility was subsequently supported by a separate investigation of the assumed and actual fatigue loads and stresses.

Contents

(27 pages in total)

1 Introduction

On 10 November, 1998, a Royal Netherlands Navy (RNLN) Lynx helicopter lost a rotor blade during preparation for take-off. The blade loss was due to failure of a rotor hub arm. Figure 1 shows the failure schematically. It occurred in the "yellow" arm of the rotor hub, a monolithic Ti-6Al-4V titanium alloy forging, across an elliptical plain section. Figure 2 is an overview of the outboard fracture surface of the failure. Concentric semi-circular ring markings, so-called "beach markings", on the fracture surface indicated fatigue failure beginning from the arrowed location. This was on the upper surface of the rotor hub arm, towards the trailing edge.

The rotor hub had accumulated 3591.9 service hours until the failure, whereas the overall design Safe-Life had been estimated as 5000 hours minimum, and the failure location Safe-Life was estimated to be 8600 hours [1]. The failure was thus unexpected and apparently very premature. In an initial response the helicopter manufacturer, GKN Westland (GKNW), suggested the most likely cause of failure was poor fatigue properties of the hub material at the failure location. This suggestion became the focus of an extensive material-based failure analysis [2].

This paper surveys the failure analysis procedure, the topics and techniques, and the results. There follows a discussion of how fractographic data from the service failure and full-scale and specimen fatigue test failures, combined with linear elastic fracture mechanics, led to estimates of certain service fatigue stresses. These estimates indicated that the service stress history could have been more severe than the fatigue stress history assumed for the design Safe-Life analysis. This possibility was later supported by a separate investigation in which GKNW made a new Safe-Life fatigue analysis that included a previously neglected service load condition called "Minimum Pitch On Ground" (MPOG) [3].

2 Failure analysis topics and techniques

Table 1 shows the scope of the material-based failure analysis in terms of the main and secondary topics and their relation to the *potential* problem areas (hub manufacture, service usage) from which the failure might be explained. In more detail, table 2 lists the techniques used to obtain information for the various topics. Two main points are to be noted here. First, the failure analysis made extensive use of the rotor hub (M323) that failed in service and a rotor hub (M6) that failed during a full-scale fatigue test. Second, both the fractography and metallography relied mainly on Scanning Electron Microscopy (SEM).

3 Survey of the results

3.1 Thermomechanical processing and heat treatment

As stated earlier, the failed rotor hub (M323) was a monolithic Ti-6Al-4V titanium alloy forging. The forging was produced from billet stock by conventional ($\alpha + \beta$) phase field working (extrusion + two die forging operations) to provide a uniformly worked $\alpha + \beta$ microstructure. This processing was followed by annealing for 3 hours at 700 °C (973 K).

Precision sectioning of *one* of the fracture surfaces, at and near the fatigue origin, was done to check the microstructural condition. This was normal, consisting of primary α and transformed β, with some bands of elongated α grains. Figure 3 is an example metallograph showing part of a band of elongated α next to more equiaxed primary α. This example also shows where checks were made for differences in primary α hardnesses and in-depth *relative* oxygen contents, using Auger Electron Spectroscopy (AES). The elongated primary α tended to have higher hardness than the equiaxed primary α, but the in-depth oxygen contents were the same [4]. Thus the smaller effective grain size of the elongated primary α was most probably the reason for its higher hardness.

The AES measurements also showed that nitrogen was not detectable within the equipment limits [4]. In view of this and the above results, it was concluded that there was no evidence for excessively hard and high-interstitial content α phase in the microstructure, and hence no indication of a fatigue-initiating metallurgical defect (see Costa *et al*. [5]).

On the other hand, independent bulk chemical analyses, subcontracted by GKNW and the RNLN, showed the oxygen content of the failed yellow arm to be 0.22-0.23 wt. %, which is above the specification maximum of 0.2 wt. %. This discrepancy required closer scrutiny, since oxygen is a strong α-stabilizer that increases the yield strength and hardness of primary α and might – in excessive amounts – decrease the fatigue strength (in the first instance an increased oxygen content appears to be generally beneficial to fatigue strength [6, 7]). However, microstructural and microhardness checks, and fatigue, tensile and fracture toughness tests [2], gave no indication that the above-maximum oxygen content could have been deleterious to the engineering properties of the failed yellow arm.

3.2 Finishing

The secondary topics listed under "Finishing" in table 1 belong to two groups. Stress-relief annealing, final machining and shot peening are the actual finishing stages, whereas the remaining topics are checks, see table 2.

The checks showed the dimensions and shot peening conformed to the specifications, and that scratches on the failed yellow arm occurred during hub manufacture. Furthermore, the scratches were not responsible for secondary cracks close to the fracture surfaces.

However, there was a finishing anomaly: a vacuum leak near the end of stress-relief annealing at 625-630 °C (898-903K). The hub manufacturer checked for oxygen contamination owing to vacuum loss. The contamination was no more than 30 μm deep and was removed during final machining. To ensure uniform removal, the hub manufacturer drilled blind flat-bottomed reference holes on all surfaces of the M323 rotor hub. These holes had to disappear during the final machining.

The failure analysis included a check to see whether one of the blind reference holes could have been at the same location as the fatigue origin in the failed yellow arm, see figure 2. It was concluded that this was improbable [2].

3.3 Service damage
Scratches arising from service damage were not observed at the failure location of the M323 rotor hub yellow arm.

Service Stress Level Estimates

Service stress level estimates were obtained from fractographic analyses and fracture mechanics concepts, as will be discussed in the next main section of this paper. The estimates were consistent in suggesting that the maximum frequently occurring alternating stress, $S_{a,mfo}$, at the failure location of the M323 yellow arm could have been well above 300 MPa, and even above 350 MPa. These are rather high values that suggest failure was due to frequently occurring fatigue stresses higher than those used in the original Safe-Life design analysis.

4 Fractographic analysis and fracture mechanics and stress level estimates

4.1 Introduction
The starting point for this section of the paper is the fracture topography at the fatigue origin of the M323 yellow arm service failure. Figure 4 gives a mesoscopic view of the fatigue origin on the inboard fracture surface. This is *optical* fractography, which is often better at showing mesoscopic features than SEM fractography. In the case of figure 4 there is a change in fracture surface roughness, visible as a transition from dark to light grey.

Similar changes in fracture topography were observed for the fatigue origins of the M6 full-scale and M323 specimen test failures. These changes were mapped using combinations of optical and SEM fractography over the magnification range $30\times - 3000\times$. Stereo pair SEM fractography was particularly useful in defining the boundaries between the changes in fracture topography: figure 5 is an example, showing the same area as in figure 4.

These boundaries between changes in fracture topography were used with some concepts from linear elastic fracture mechanics to obtain estimates of fatigue stress levels for the service failure. Two essentially independent methods were used: (1) comparison between the M323 service failure and M6 full-scale test failure; and (2) comparison between the M323 service failure and specimen failures.

4.2   Method (I): Comparison of Service and Full-Scale Test Failures

Figure 6 compares schematics of the fatigue origin areas of the service and full-scale test failures. Fatigue nucleation was subsurface owing to surface shot peening (though titanium alloys can show naturally-occurring subsurface fatigue origins at very long lives). Thus the fatigue cracks grew initially in vacuo. When the cracks broke through to the outer surfaces there was a subtle but definite change in fracture topography, namely that the fatigue facets produced in air were more sharply defined than those produced in vacuo. Figure 7 gives an example of this difference, whereby it should be noted that the SEM magnification for the facet produced in air is twice that for the facet produced in vacuo.

Of more importance in the present context is the fracture roughness transition boundary, visible in figures 4 and 5 for the service failure, and also found for the full-scale test failure [2]. Figure 6 shows that the crack sizes at each fracture topography change were smaller for the full-scale test. This difference is consistent with the full-scale fatigue stress levels being generally higher than those for the service failure. Table 3 shows the full-scale fatigue stress levels at the fatigue origin in rotor hub arm 4C, which failed after approximately 7×10^5 cycles, representing 175 flying hours [8]: this was evidently an accelerated test.

There were two other differences between the service and full-scale test failures:

(1)   The fatigue origins were respectively on the upper and lower surfaces of the rotor hub arms. However, in both cases the fatigue origins corresponded to known positions of fatigue stress maxima [2].

(2)   The service failure location was about 8 mm outboard of the full-scale test failure location. This difference is negligible with respect to the bending moments on the rotor hub arms [8].

In view of the above-appended comments on these two differences, it was concluded that the service and full-scale test failures could be directly compared with respect to their fatigue stress histories.

4.2.1   Method (I) Basic Estimate

Wanhill and Looije [9] showed experimentally that the fracture roughness transition boundary most probably corresponds to the maximum plane-strain cycle plastic zone dimension becoming equal to the primary α average grain size in ($\alpha+\beta$) processed Ti-6Al-4V. The maximum plane-strain cyclic plastic zone dimension is given by

$$r_y^c = \left(0.05\,\Delta K_{eff}\,/\,\sigma_y^c\right)^2 \tag{1}$$

where ΔK_{eff} is the effective stress intensity factor range in fatigue, and σ_y^c is the cyclic yield stress of the material. Further,

$$\Delta K_{eff} = \Delta S_{eff}\,\sqrt{\pi a}\,(Y) \tag{2}$$

Where ΔS_{eff} is the effective fatigue stress range, a is the crack size, and Y is a geometric factor dependent on crack shape and size and component shape and size. We now assume the following equalities between the M323 and M6 failure locations:

(1)   Same primary α average grain size. This is reasonable, since the primary α mean grain sizes were similar for all investigated rotor hubs [2].

(2)   Same cyclic yield stress. This is reasonable owing to the same thermomechanical processing and heat treatment and the similar primary α grain sizes.

(3)   Same value of Y. This is reasonable, firstly because the fatigue cracks were both approximately semi-circular at the fracture roughness transition boundary, see figure 6, and secondly because the crack sizes at this boundary are so small that the arm cross-sectional geometry would have had no influence on Y.

(4)   Same fatigue stress ratio, $R = S_{min}/S_{max}$. Since the failures did not initiate at the same position, this assumption could well be incorrect. But, as will be argued later, any discrepancy is likely to be of minor importance.

With these assumptions we may write

$$\left(\Delta S_{eff} \sqrt{a}\right)_{M323} = \left(\Delta S_{eff} \sqrt{a}\right)_{M6} \tag{3}$$

At the fracture roughness transition boundary the crack depths, a, were 1.02 mm for the M323 failure and 0.78 mm for the M6 failure, see figure 6. Substituting these values in equation (3) gives

$$\left(\Delta S_{eff}\right)_{M323} = 0.87 \left(\Delta S_{eff}\right)_{M6} \tag{4}$$

To proceed further we need to make the following additional assumption:

(5) For the M6 full-scale test the fracture roughness transition boundary was determined by the level 3 fatigue stresses, see table 3. The choice of level 3 is based on Wanhill and Looije [9], who showed experimentally that it is the maximum value of the *frequently occurring* fatigue stresses that determines the fracture roughness transition boundary. Level 3 occurred as about 12 % of the total cycles, which is considered fairly frequent, while level 4 was most infrequent.

For the M6 fatigue origin it was therefore assumed that the maximum frequently occurring alternating stress, $S_{a,mfo}$, was 426 MPa. Then provided assumptions (1) – (5) are *all* valid, the equivalence represented by equation (4) leads to the following basic estimate of $S_{a,mfo}$ for the M323 fatigue origin:

basic estimate $(S_{a,mfo})_{M323} = 0.87 \,(426 \text{ MPa}) \quad = 371 \text{ MPa}$

4.2.2 Method (I) Modified Estimates
Additional estimates of $S_{a,mfo}$ can be made whereby the assumptions (1) and (4) for the basic estimate are considered invalid, either separately or together.

(1) *Grain size.* If we assume a 20 % smaller average grain size for the primary α in the M323 yellow arm (a conservative assumption [2]), then since r_y^c at the fracture roughness transition boundary will scale linearly with the grain size, we may write from equations (1) – (4)

$$\left(\Delta S_{eff} \sqrt{a}\right)_{M323} = \sqrt{0.8} \left(\Delta S_{eff} \sqrt{a}\right)_{M6} \tag{5}$$

and

$$\left(\Delta S_{eff}\right)_{M323} = \sqrt{0.8} \; (0.87)\left(\Delta S_{eff}\right)_{M6} \tag{6}$$

Provided the remaining assumptions (2) – (5) for the basic estimate are valid, then the equivalence represented by equation (6) leads to a second estimate of $S_{a,mfo}$ for the M323 fatigue origin:

second estimate	$(S_{a,mfo})_{M323}$ = 332 MPa

(2) *Stress ratio*. The value of R for the M6 fatigue origin was –0.59 [2,8]. It is possible that the M323 fatigue origin had a similar R value. However, we shall here assume the most different R value that could be obtained for the M323 fatigue origin from the combinations of mean and alternating stresses used in the full-scale test and thought to be representative of service [8]. This R value is –1.14 [2,8]. Using Newman's plane-strain crack closure model [10], we may write the following expression for negative R values:

$$\Delta S_{eff} = S_{max} (0.75 - 0.078 \, R) \tag{7}$$

whence

$$(\Delta S_{eff})_{M323} = 0.84 \; (S_{max})_{M323} \; ; \; (\Delta S_{eff})_{M6} = 0.80 \; (S_{max})_{M6}$$

We now have to make an additional assumption that is not obvious, namely that the equivalence represented by equation (3) is valid for differing R. As will be shown during the Method (2) estimates, this assumption is reasonable for R values ranging from –0.59 to –1.14. With this additional assumption, substitution of $(S_{max})_{M323}$ and $(S_{max})_{M6}$ into equations (4) and (6) gives:

equal grain size	$(S_{max})_{M323} = \dfrac{0.80}{0.84} \; 0.87 \; (S_{max})_{M6} = 0.83 \; (S_{max})_{M6}$	(8)

unequal grain size	$(S_{max})_{M323} = 0.83 \; \sqrt{0.8} \; (S_{max})_{M6} = 0.74 \; (S_{max})_{M6}$	(9)

Provided the remaining assumptions not covered by equations (8) and (9) are valid, i.e. the assumptions (2), (3) and (5) for the basic estimate, and recognising that for any S_{max} the S_a

value is 0.5 S_{max} (1-R), then the equivalences represented by equations (8) and (9) lead to third and fourth estimates of $S_{a,mfo}$ for the M323 fatigue origin:

| third estimate |

$(S_{a,mfo})_{M323} =$ 1.12   (426 MPa) =   477 MPa

| fourth estimate |

$(S_{a,mfo})_{M323} =$ 1.00   (426 MPa) =   426 MPa

4.3   Method (II) Comparison of Service and Specimen Test Failures

GKNW supplied the NLR with fracture halves of three cylindrical fatigue specimens taken from the M323 failed yellow arm. The specimens had been shot peened to the same specification as the rotor hub arm. The fatigue test information is given in table 4. The cycle frequency was 152 Hz.

Figure 8 shows schematics of the fatigue origin areas of the specimens. The fracture roughness transition boundaries were visible, but details within these boundaries were largely obscured by fretting debris and hammering of the fracture surfaces as a consequence of fully reversed stressing (R = -1). This behaviour was not observed for the M323 service failure and M6 full-scale test failure. In turn, this indicates that in *both* cases the local R value was much less negative than R = -1. Thus it is possible that the M323 fatigue origin R value was similar to that for the M6 fatigue origin, as mentioned with respect to the Method (1) modified estimates.

Since the specimens were cylindrical, the fracture roughness transition boundaries approximated to the configuration of semi-elliptical cracks in round bars. There is no straightforward stress intensity factor solution for this configuration, but Murakami's Handbook [11] gives functional relationships for certain values of a/c, a/r and c/r, where a, c and r are shown in figure 8. The Handbook results closest to the configurations in figure 8 are summarised in figure 9, where we assume a/c = 1. The actual a/c values were 1.15, 1.23 and 1.29, but there are no Handbook data for a/c > 1. We assume further that the dimensionless stress intensity factors, F_1, in figure 9 apply to the specimen crack sizes and shapes at the fracture roughness transition boundaries. Interpolation of the functional relationship in figure 9 then gives the results in table 5. The constancy of the $K_{max,T}$ values in table 5 is evidence for fracture mechanics control of the roughness transition boundaries.

Further necessary information is obtainable by converting $K_{max,T}$ to $\Delta K_{eff,T}$. This may be done using equation (7) and taking the specimens' R value of –1. The average result is $\Delta K_{eff,T} = 15.3$ MPa$\sqrt{m}$. Figure 10 compares this result with $\Delta K_{eff,T}$ values obtained for similarly processed Ti-6Al-4V [9]. From what is generally known about stress ratio effects on fatigue crack growth

rates (see e.g. Newman [10]), figure 10 shows a plausible functional dependence of $\Delta K_{eff,T}$ on R. The consequences of this plausibility are twofold:

(a) It supports the assumption that the fracture roughness transition boundaries for the M323 and M6 rotor hub arms and the M323 fatigue specimens are due to the same mechanism.

(b) At the fracture roughness transition boundary the equivalence represented by equation (3) is strictly valid only for the same R.

Although point (b) might seen problematical, figure 10 shows there is little change in $\Delta K_{eff,T}$ over a wide range of negative R. Returning to the question of stress ratio differences discussed for the Method (I) modified estimates, from figure 10 we obtain $\Delta K_{eff,T}$ values of 15.3 MPa $\sqrt{m}$ and 15.0 MPa $\sqrt{m}$ for R = –1.14 and R = –0.59 respectively. This difference in $\Delta K_{eff,T}$ values van be neglected in the present context of service stress level estimates.

We are now in a position to estimate the service failure fatigue stresses using the specimen test failures and making the following assumptions:

(1) The fracture roughness transition boundaries for the M323 service failure and fatigue specimens are due to the same mechanism.

(2) The $\Delta K_{eff,T}$ versus R relationship in figure 10 is valid for the M323 fatigue specimens and service failure: in the latter case specifically with respect to $(S_{a,mfo})_{M323}$ for the fatigue origin location.

(3) For the M323 service failure we may use the approximate stress intensity factor for a semi-circular surface crack in a thick plate [12]:

$$K_I = 2.24 \, S \sqrt{\pi a} \, / \, \pi \tag{10}$$

where a is the crack depth at the fracture roughness transition boundary.

For the M323 service failure the fracture roughness transition boundary occurred at a = 1.02 mm, as mentioned earlier. We now substitute $\Delta K_{eff,T}$ for K_I, ΔS_{eff} for S and a = 1.02 mm (= 0.00102 m) in equation (10) to obtain a general expression independent of R:

$$\Delta K_{eff,T} = 2.24 \, \Delta S_{eff} \, \sqrt{\pi(0.00102)} \, / \, \pi \tag{11}$$

We use equation (11), the $\Delta K_{eff,T}$ versus R relationship in figure 10, and equation (7) to derive $\Delta K_{eff,T}$, S_{max}, S_{min}, and $(S_{max} - S_{min}) / 2 = (S_{a,mfo})_{M323}$ for selected values of R, see table 6. As discussed earlier, it is likely that the M323 fatigue origin R value was much less negative than R = -1 and possibly the same as that for the M6 fatigue origin, i.e. R = -0.59. On this basis, table 6 indicates a reasonable estimate of $(S_{a,mfo})_{M323}$ = 372 MPa.

5 Discussion of the $(S_{a,mfo})_{M323}$ estimates

Two essentially independent methods of estimating fatigue stress levels for the M323 service failure have been presented in the foregoing sub-sections of this paper. These methods share only one assumption without question or discussion, namely that the cyclic yield stress, σ_y^c, was the same in all cases, which is reasonable.

Method I resulted in estimates of $(S_{a,mfo})_{M323}$ varying from 332 MPa to 477 MPa for the fatigue origin location in the M323 failed rotor hub arm. Method II indicated firstly that the fatigue stress ratio was much less negative than R = -1 for the fatigue origin location of the M323 failed rotor hub arm. Secondly, a plausible value of R = -0.59 resulted in the estimate $(S_{a,mfo})_{M323}$ = 372 MPa.

The very close agreement between the basic estimate of $(S_{a,mfo})_{M323}$ from method I and the intermediate estimate from method II is fortuitous. However, the general agreement between the results of both methods, knowing that R = -0.59 is plausible, suggests that the maximum frequently occurring alternating stress $(S_{a,mfo})_{M323}$ at the fatigue origin location of the M323 failed rotor hub arm was well above 300 MPa.

$(S_{a,mfo})_{M323}$ values above 300 MPa are high with respect to the rotor hub design Safe-Life analysis. For example, the fatigue endurance limit estimates for the M323 service failure location ranged from 299 MPa to 342 MPa [3]. The question now arises: how likely is it that high values of $S_{a,mfo}$ were indeed responsible for the M323 service failure? This is discussed, albeit summarily, in the next section.

6 Supplementary measurements of service loads and fatigue analysis

During and after the material-based failure analysis of the M323 rotor hub, GKNW investigated all the service load conditions that could possibly be relevant to the accident. A particular ground load condition, designated Minimum Pitch On Ground (MPOG), was found capable of

including fatigue stresses above the rotor hub endurance limit. Furthermore, this load condition had not been included in the rotor hub design Safe-Life analysis.

Accordingly, GKNW developed an MPOG load model to estimate the fatigue damage rate of the rotor hub owing to this load condition [13]. Several assumptions were made about operation of the RNLN Lynx helicopters. A notable assumption in the present context is the average time of 7 minutes MPOG per flight hour. For a reasonably constant rotor speed this corresponds to about 11 % of the total cycles, which is remarkably close to the level 3 occurrences in the M6 full-scale test, see table 3; and it will be recalled that the choice of level 3 to represent $S_{a,mfo}$ is a key assumption for the method I estimate of service stresses for the M323 service failure.

Using the well-known Palmgren-Miner cumulative damage hypothesis, also used in the original Safe-Life analysis, GKNW found that the MPOG load condition for RNLN Lynx helicopters could have contributed up to 70 % of the total fatigue damage to the rotor hub [3, 13]. Here, then, is a strong indication that the MPOG load condition corresponds to high values of $S_{a,mfo}$, and that these high values were primarily responsible for the M323 service failure. One last point is that it is irresistibly tempting to suggest that the MPOG load condition was also responsible for final (overload) fracture of the yellow rotor hub arm while the helicopter was preparing to take off.

7 Conclusions

Fatigue and fracture of a titanium alloy Ti-6Al-4V rotor hub arm from a Royal Netherlands Navy Lynx helicopter resulted in an extensive material-based failure analysis. The failure analysis covered manufacture of the hub, service damage and estimates of service stresses. These estimates were obtained from fractographic analyses and elementary fracture mechanics concepts.

The results of the failure analysis led to two main conclusions:

(1)   There was no evidence for failure of the rotor hub arm owing to poor material properties.

(2)   Failure was most probably due to frequently occurring service fatigue loads and stresses higher than those used in the original design Safe-Life analysis.

A supplemental investigation of service loads, followed by a new fatigue design analysis, gave results supporting conclusion (2).

8 Acknowledgements

9 References

1. J.M. Falconer and P.N. Goddard, GKN Westland Helicopters letter JMF/KP/1036 to the Royal Netherlands Navy, 14 November 1998.
2. GKN Westland, KIM (RNLN) and NLR, "Material-Based Failure Analysis of the Lynx-282 Rotor Hub", NLR-CR-99189, National Aerospace Laboratory NLR, Amsterdam, the Netherlands, March 2000.
3. J. Laméris, "Review of the Fatigue Analysis of the RNLN Lynx Main Rotor Head", NLR-CR-2000-193, National Aerospace Laboratory NLR, Amsterdam, The Netherlands, April 2000.
4. J.T. de Vrij and H.J. van der Mijle Meijer, "Investigation of the Microstructure and Hardness of the Broken Rotor Hub from the Lynx-282 Helicopter" (in Dutch), Report 1999-7, Royal Netherlands Naval College Marine Materials Laboratory, Den Helder, the Netherlands, March 1999.
5. J.G. Costa, R.E. Gonzalez, R.E. Guyotte, D.P. Salvano. T. Swift and R.J. Koenig, "Titanium Rotating Components Review Team Report", United States of America Federal Aviation Administration, Aircraft Certification Service, Engine and Propeller Directorate, Volume 1, Public Report, 14 December 1990.
6. G. Lütjering, A. Gysler and J. Albrecht, "Influence of Microstructure on Fatigue Resistance", *Fatigue '96*, Editors G. Lütjering and H. Nowak, Elsevier Science Ltd., Oxford, UK, 1996, pp. 893-904.
7. L. Wagner, "Fatigue Life Behaviour", *ASM Handbook Volume 19, Fatigue and Fracture,* Editor S.R. Lampman, ASM International, Materials Park, OH, Second Printing, 1997, pp. 837-845.

8. R. Jabouille, "Fatigue Test of the Main Monobloc Titanium Rotor Hub" (in French), Aerospatiale Bureau D'Études Hélicoptères Document WG 13 6005, Marseilles, France, 29 March 1974.

9. R.J.H. Wanhill and C.E.W. Looije, "Fractographic and Microstructural Analysis of Fatigue Crack Growth in Ti-6Al-4V Fan Disc Forgings", AGARD Report 766 (Addendum), Advisory Group for Aerospace Research and Development, Neuilly-sur-Seine, France, April 1993, pp. 2-1 – 2-40.

10. J.C. Newman, Jr, "A Crack-Closure Model for Predicting Fatigue Crack Growth Under Aircraft Spectrum Loading*, Methods and Models for Predicting Fatigue Crack Growth Under Random Loading*, Editors J.B. Chang and C.M. Hudson, ASTM STP 748, American Society for Testing and Materials, Philadelphia, PA, 1981, pp. 53-84.

11. Y. Murakami, *Stress Intensity Factors Handbook*, Editors Y. Murakami, S. Aoki, H. Miyata, K. Tohgo, N. Hasebe, N. Miyazaki, M. Toya, Y. Itoh, H. Terada and R. Yuuki, Pergamon Press, New York, NY, Volume 2, 1987, p. 661.

12. J.A. Bannantine, J.J. Comer and J.L. Handrock, *Fundamentals of Metal Fatigue Analysis*, Prentice-Hall, Inc., Englewood Cliffs, NJ, 1990, p. 95.

13. S.P. King, "Lynx Hub MPOG Fatigue Damage Assessment", Issue 1, Report CD/SPK/ JTWP20-3555, GKN Westland Helicopters Limited, Yeovil, UK, 15 November 1999.

Table 1 The failure analysis topics

Failure analysis topics and classification	
Hub manufacture	• **Thermomechanical processing and heat treatment** 　• metallurgical defects 　• microstructural factors influencing fatigue 　• chemical composition
	• **Finishing** 　• stress relief anneal 　• final machining 　• shot peening 　• dimensions 　• residual stress measurements 　• scratches 　• scratches and secondary cracks
Service	• **Service damage** 　• scratches 　• scratches and secondary cracks • **Service stress level estimates** 　• service failure versus full-scale fatigue test 　• service failure versus specimen fatigue tests

Table 2 Failure analysis techniques and purposes

- **Documentation**
  - rotor hub production, microstructures, mechanical properties (including fatigue), chemical composition
  - hub finishing, especially stress relief annealing (*in vacuo*) and final machining procedure
  - full-scale fatigue test data, M6 hub, simple spectrum loading
  - *ad hoc* literature review of fatigue in α-β titanium alloys
- **Testing**
  - high-cycle fatigue of unnotched shot peened specimens
  - tensile and fracture toughness properties } M323 rotor hub failed yellow arm
- **Fractography: service failure, full-scale and specimen fatigue test failures**
  - fatigue origins, fracture characteristics (micromechanisms), mesoscopic topography changes
  - shot peening influence (compressive stresses in surface layers)
  - EDX chemical analysis of service failure fatigue origin
- **Metallography: service failure, full-scale fatigue test failure, other rotor hubs**
  - precision sectioning of service failure fatigue origin to look for metallurgical defects
    - microstructures, microhardness, Auger Electron Spectroscopy for oxygen and nitrogen contents
  - microstructures and microhardness checks on M323, M6 and other hub arms
    - primary α grain size, percentages of α and β
  - depth of shot peening on M323 rotor hub failed yellow arm (interference light microscopy)
  - secondary cracks and fracture surface profiles for the service failure
- **Other checks**
  - dimensions of M323 failed rotor hub and M317 rotor hub arms after final machining
  - bulk chemical composition
  - shot peening residual stresses } near outboard fracture surface of M323 rotor hub failed yellow arm
  - scratches on the M323 and M317 rotor hub arms and their relation to
    - standard finishing (machining, shot peening, etching, anodising)
    - secondary cracks close to the M323 failure location (fracture surfaces)

Table 3 M6 full-scale test fatigue stresses at the fatigue origin in arm 4C

Level	Sa (MPa)	Cycles per "flight"hour	% total cycles
1	287	2420	60.5
2	360	1090	27.3
3	426	483	12.1
4	512	6	0.15

Table 4 Specimen fatigue test information (R = -1)

Specimen	Stress, S(MPa)	Cycles to Failure
LT6MDF35	0 ± 300	4.2×10^7
LT6MDF36	0 ± 275	4.8×10^7
LT6MDF37	0 ± 250	6.2×10^7

Table 5 Stress intensity factors at point A on the specimen fracture roughness transition boundaries

Specimen	$K_{max,T} = F_1 S_{max} \sqrt{\pi a}$ $(MPa\sqrt{m})$
LT6MDF35	18.6
LT6MDF36	18.4
LT6MDF37	18.4

Table 6 Dependence of $(S_{a,mfo})_{M323}$ on R

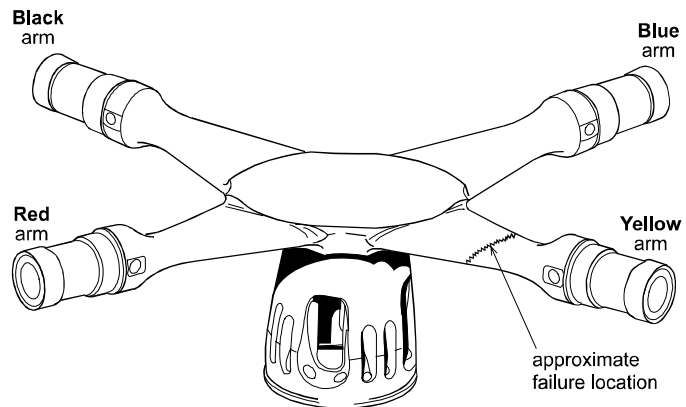| R	$\Delta K_{eff,T}$ $(MPa\sqrt{m})$	ΔS_{eff} (MPa)	S_{max} (MPa)	S_{min} (MPa)	$(S_{a,mfo})_{M323}$ (MPa)
-1.14	15.3	379	452	-515	484
-0.59	15.0	372	467	-276	372
0	13.3	330	440	0	220

Fig. 1   Failure location in the monolithic rotor hub, a Ti-6Al-4V forging

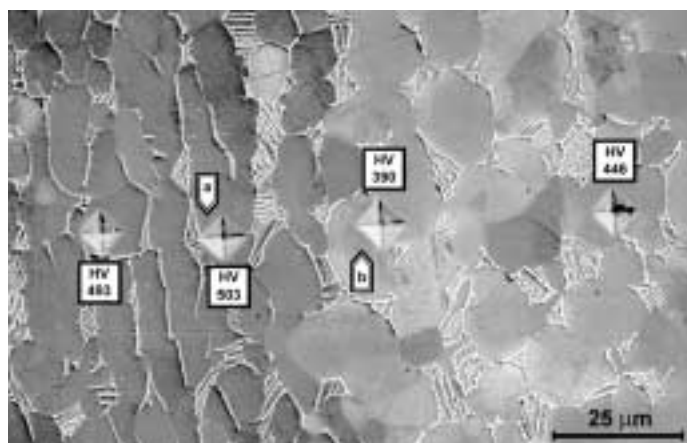Fig. 2   Macrophotograph of the yellow arm outboard fracture surface. The failure origin is arrowed

Fig. 3   SEM micrograph near the M323 fatigue origin, showing the $\alpha + \beta$ microstructure, microhardness (HV) measurements in primary α grains, and locations (a, b) analysed for oxygen content using Auger Electron Spectroscopy (AES)
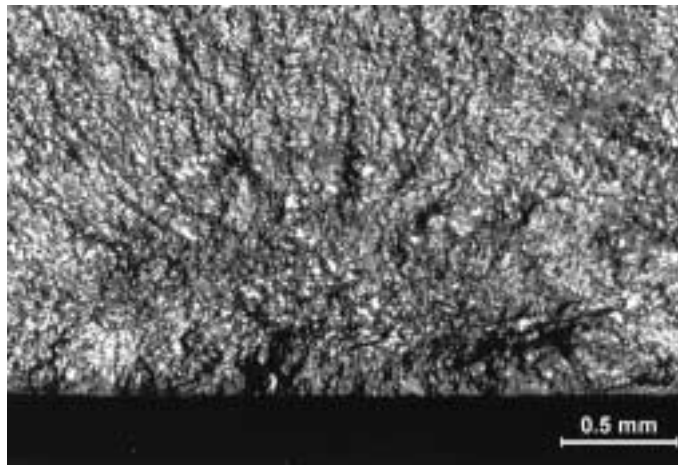
Fig. 4   Mesofractograph of the fatigue origin on the inboard fracture surface of the M323
service failure, showing a change in roughness (dark to light grey)
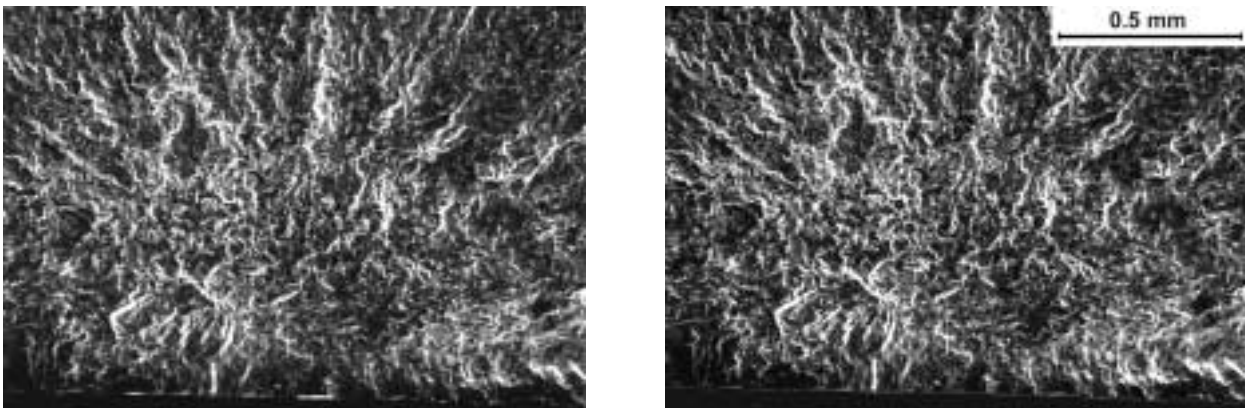

Fig. 5   Stereo pair SEM mesofractographs of the fatigue origin on the inboard fracture of the M323
service failure: y-axis tilt ± 5 , some vertical foreshortening due to x-axis tilt for better visibility
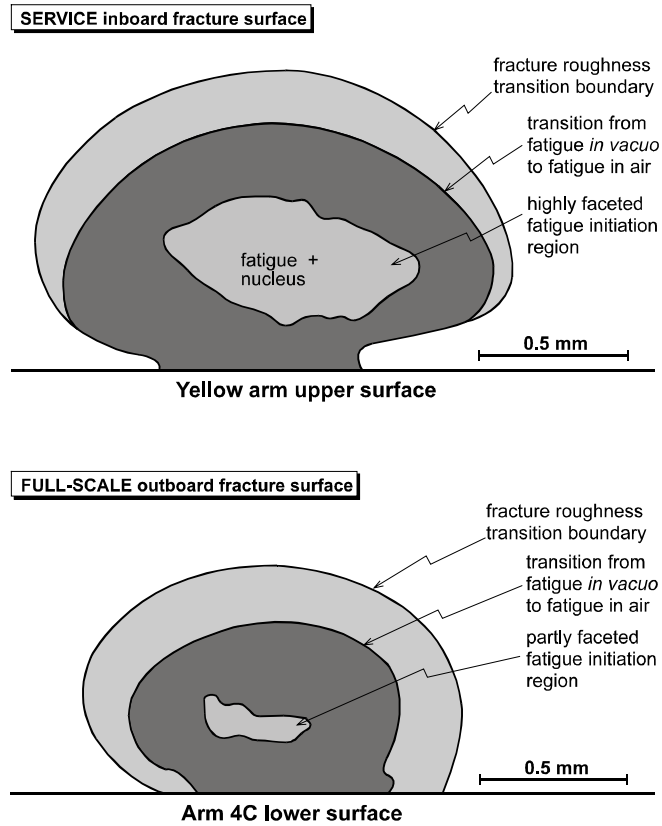of topography changes

SERVICE inboard fracture surface

fracture roughness
transition boundary

transition from
fatigue *in vacuo*
to fatigue in air

highly faceted
fatigue initiation
region

fatigue +
nucleus

0.5 mm

Yellow arm upper surface

FULL-SCALE outboard fracture surface

fracture roughness
transition boundary

transition from
fatigue *in vacuo*
to fatigue in air

partly faceted
fatigue initiation
region

0.5 mm

Arm 4C lower surface

Fig. 6   Schematics of the fatigue origin areas of the M323 service and M6 full-scale test failures

local crack growth direction

local crack growth direction

Fatigue *in vacuo*
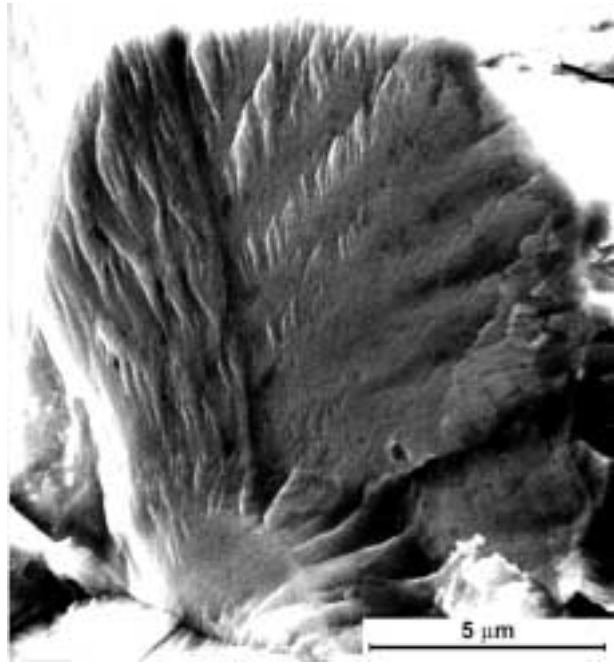
Fatigue in air

Fig. 7   Microfractographic differences between fatigue facets produced in vacuo *and in air*
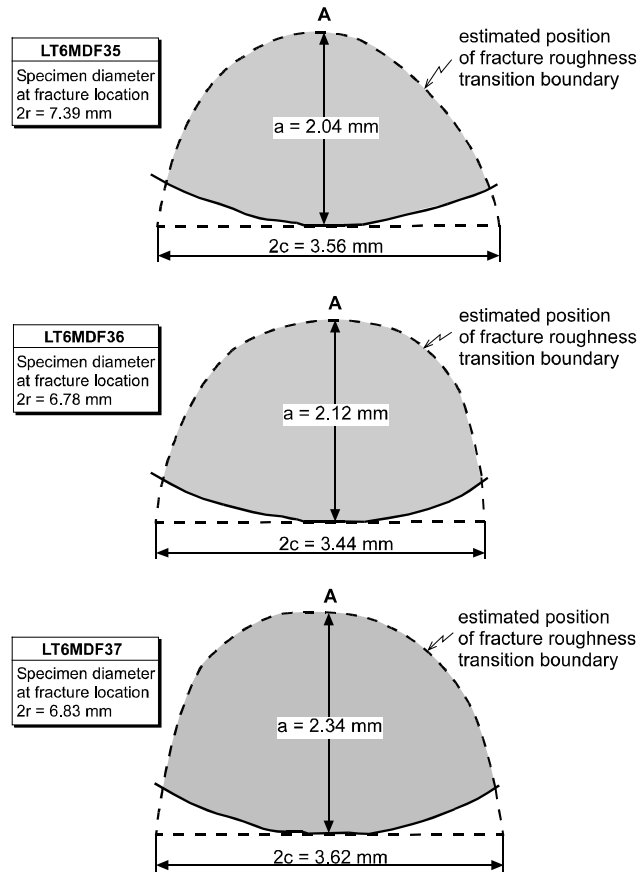*These details are SEM fractographs of the fatigue origin area of the M323 service failure*

Fig. 8   Schematics of the fatigue origin areas of the three failed specimens LT6MDF35-37.
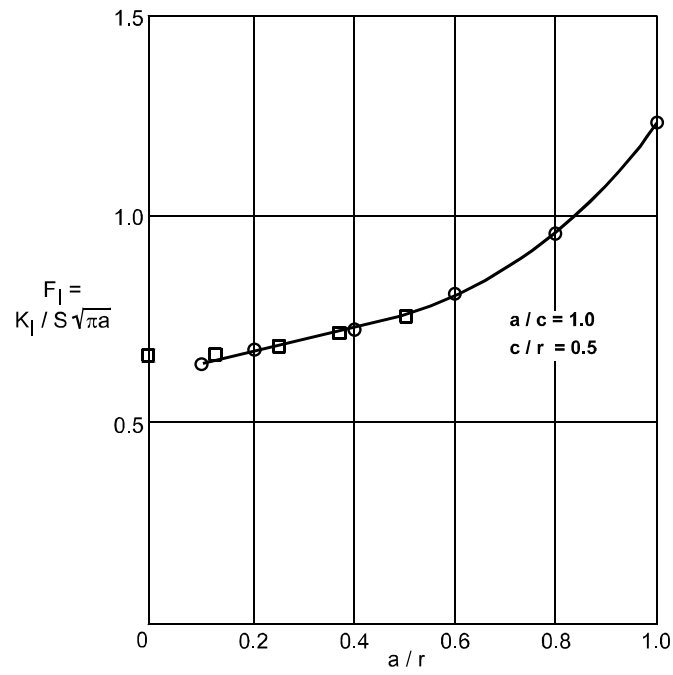Dimensions were obtained from SEM fractographs

Fig. 9   Dimensionless stress intensity factors, F_I, at point A (see figure 8) for semi-elliptical cracks in tension-loaded round bars. After Murakami [11]
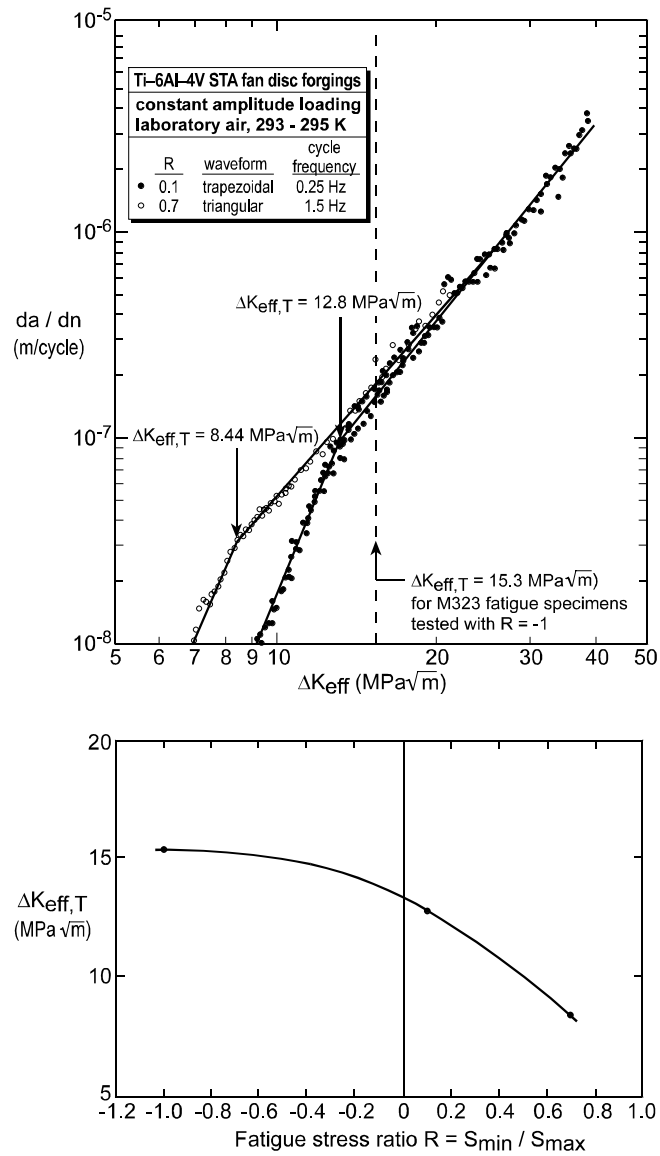
Fig. 10 *Functional dependence of $\Delta K_{eff, T}$ on R. The fatigue crack growth data are from Wanhill and Looije [9]*